PAPER

Three-dimensional corrugation of the plasma edge when magnetic perturbations are applied for edge-localized mode control in MAST

Plasma Phys. Control. Fusion **54** (2012) 105013 (9pp) doi:10.1088/0741-3335/54/10/105013

Three-dimensional corrugation of the plasma edge when magnetic perturbations are applied for edge-localized mode control in MAST

I T Chapman[1], W A Cooper[2], A Kirk[1], C J Ham[1], J R Harrison[1], A Patel[1], S D Pinches[1], R Scannell[1], A J Thornton[1] and the MAST Team

[1] Euratom/CCFE Fusion Association, Culham Science Centre, Abingdon, OX14 3DB, UK
[2] Ecole Polytechnique Fédérale de Lausanne (EPFL), Centre de Recherches en Physique des Plasmas, Association Euratom-Confédération Suisse, CH-1015 Lausanne, Switzerland

E-mail: ian.chapman@ccfe.ac.uk

Received 25 May 2012, in final form 8 August 2012
Published 5 September 2012
Online at stacks.iop.org/PPCF/54/105013

Abstract
The distortion of the plasma boundary when three-dimensional resonant magnetic perturbations (RMPs) are applied has been measured in MAST H-mode plasmas. When the $n = 3$ RMPs are applied to control edge-localized modes (ELMs), the plasma experiences a strong toroidal corrugation. The displacement of the plasma boundary is measured at various toroidal locations and found to be of the order of 5% of the minor radius for an applied field magnitude which mitigates ELMs. The empirically observed corrugation of the plasma edge position agrees well with three-dimensional ideal plasma equilibrium reconstruction.

(Some figures may appear in colour only in the online journal)

1. Introduction

When tokamak plasmas operate in a high-confinement regime, the plasma edge can be susceptible to quasi-periodic instabilities called edge-localized modes (ELMs) [1]. These ELMs are understood to be a manifestation of so-called peeling–ballooning instabilities driven by strong pressure gradients and localized current density at the edge of the plasma [2, 3]. Although it is desirable to operate tokamak plasmas in the high-confinement regime to maximize fusion yield, the resultant ELMs can eject potentially damaging levels of energy and particles from the confined region, making them a concern for the lifetime of plasma facing components [4]. In order to avoid damage to vessel components in ITER a robust ELM control scheme is required to suppress the ELMs completely or, at least, to reduce the energy loss per ELM by at least an order of magnitude [5]. One such control scheme is the application of resonant magnetic perturbations (RMPs), which perturb the magnetic field in the edge transport barrier, or pedestal, region. RMPs have been applied to completely suppress ELMs in DIII-D [6, 7] and KSTAR [8], or to mitigate ELMs—that is to say increase their frequency and reduce their amplitude—in ASDEX Upgrade [9], MAST [10] and JET [11]. Whilst this ELM control actuator clearly involves imposing a non-axisymmetric perturbation to the magnetic field, the plasma is still often treated two dimensionally in equilibrium reconstruction and stability analyses [7, 12–15].

In an ideal axisymmetric diverted magnetic configuration, the separatrix, or last-closed flux surface (LCFS), separates the closed field lines that confine the plasma, and the open field lines. The application of non-axisymmetric RMPs has been predicted to cause a deformation of the separatrix, which can lead to significantly radially extended structures near to the X-point [16, 17]. This deformation of the separatrix was recently observed for the first time using visible-light imaging on MAST [18]. The lobe structures observed when RMPs are applied, as seen clearly in [18], were predicted as manifestations of the homoclinic tangle which replaces the separatrix when the magnetic field is perturbed [16]. Non-axisymmetric magnetic perturbations were predicted to split the separatrix into stable and unstable manifolds [17], with corrugated structures forming where these manifolds intersect. These homoclinic tangles are computed to be particularly complex and extended near the X-point. This concept of lobe

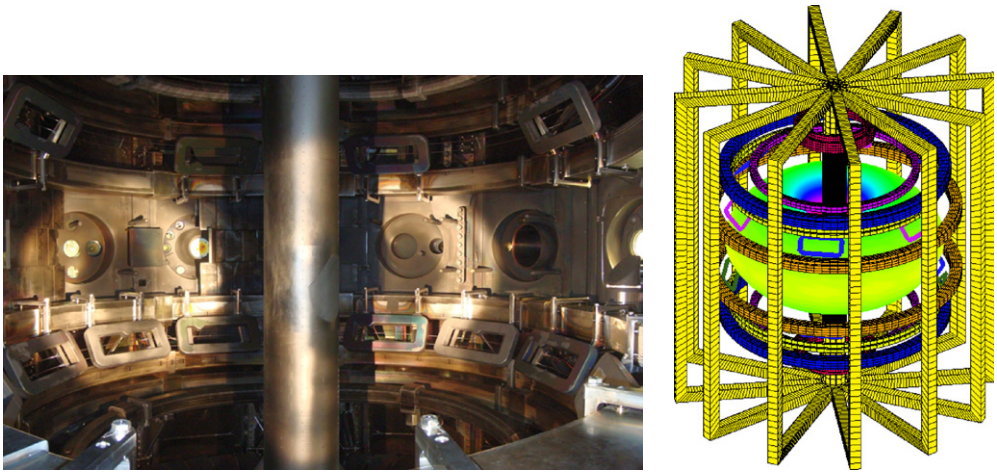

Figure 1. A photograph of the in-vessel coils in the MAST torus and a schematic of the MAST toroidal field, poloidal field and in-vessel coils set.

structures formed by the invariant manifolds of the perturbed field has been used to explain the splitting of the divertor leg footprints observed on strike-point targets during RMP experiments [16, 19–23].

Previous experiments to measure the plasma perturbation when non-axisymmetric perturbation fields are applied have been performed on DIII-D [24, 28], ASDEX Upgrade [25, 26] and MAST and JET [27]. In some DIII-D discharges the plasma response to $n = 1$ fields was found to amplify the edge perturbation [24], whilst in both MAST and JET L-mode plasmas and other DIII-D cases with $n = 3$ RMPs [28], the displacement of the edge of the plasma scaled approximately linearly with the applied field. Nonetheless, in all cases, applied fields from either ex- or in-vessel field correction coils had a demonstrable and significant effect on the toroidal periodicity of the plasma edge, deforming the separatrix by a few per cent of the minor radius.

Whilst two-dimensional treatment of the plasma equilibrium is routine, it should be noted that three-dimensional plasma equilibrium reconstruction when RMPs were applied has been performed for JET [29], TEXTOR [30] and NSTX [31]. In order to fully understand how RMPs change the stability properties of the edge of the plasma to lead to ELM suppression [7, 8] or ELM mitigation [9–11], it is important to take into account these three-dimensional corrugations of the plasma edge when RMPs are applied. MAST is able to assess this non-axisymmetric perturbation of the plasma as it has diagnostics with an ability to measure the position of the plasma edge with sub-centimetre spatial resolution in multiple toroidal sectors. MAST is also equipped with 18 in-vessel ELM control coils for applying RMPs. This coil set consists of two rows of coils mirrored about the midplane, the upper row containing six equally spaced coils, and the bottom row comprising twelve coils. This flexible coil set allows the application of RMP fields with toroidal mode number $n = 1$–6, giving rise to the first observation of ELM mitigation with $n > 3$ RMPs [18]. In order to consider the non-axisymmetric corrugation of the plasma equilibrium when ELMs are mitigated, the radial displacement of the plasma midplane has been measured using multiple high-resolution diagnostics when $n = 3$ RMPs are applied in MAST. The diagnostic set and the equilibrium configuration is described in section 2, after which measurements from these diagnostics when RMPs are applied are presented in section 3. The perturbation of the plasma edge is then compared with three-dimensional equilibrium reconstruction by the ANIMEC code [33, 34] in section 4.

2. Diagnostics and experimental configuration

MAST's in-vessel coils can be seen in figure 1 both in a photograph of the vessel interior and in a schematic drawing of the complete MAST coil set, showing the poloidal field coils and small in-vessel ELM control coils within the rectangular toroidal field coils. The effect of applying perturbations with different toroidal mode numbers has been investigated here in MAST double-null diverted (DND) plasmas optimized for diagnostic coverage. It should be noted at this point that the equilibrium separatrix splitting is complicated with two X-points; double-null plasmas demonstrate particularly complex sequences of tangle bifurcations as the up–down symmetry of the X-points is varied over a relatively small range [16]. The application of $n = 3$ RMPs results in a significant increase in type-I ELM frequency, as illustrated in figure 2, and a reduction in the energy lost per ELM whilst $n = 4$ RMPs have little effect on ELM behaviour, at least in the double-null plasma reported here.

Figure 3 shows the toroidal position of a sub-set of diagnostics useful for this study on MAST. There are twelve sectors equipped with diagnostics between the twelve toroidal field coil limbs. The primary diagnostics used to measure the radial position of the edge of the plasma are (moving clockwise from the top in figure 3) the linear D_α camera which sees the edge of the plasma with a tangency plane in sector 12; the phantom colour camera which is tangent to sector 1; the charge exchange recombination spectroscopy diagnostic which views the neutral beam in sector 6; the RGB camera which views a tangency plane in sector 7; a charge-coupled device (CCD) camera viewing with a tangency plane approximately in sector 9; and the Thomson scattering (TS)

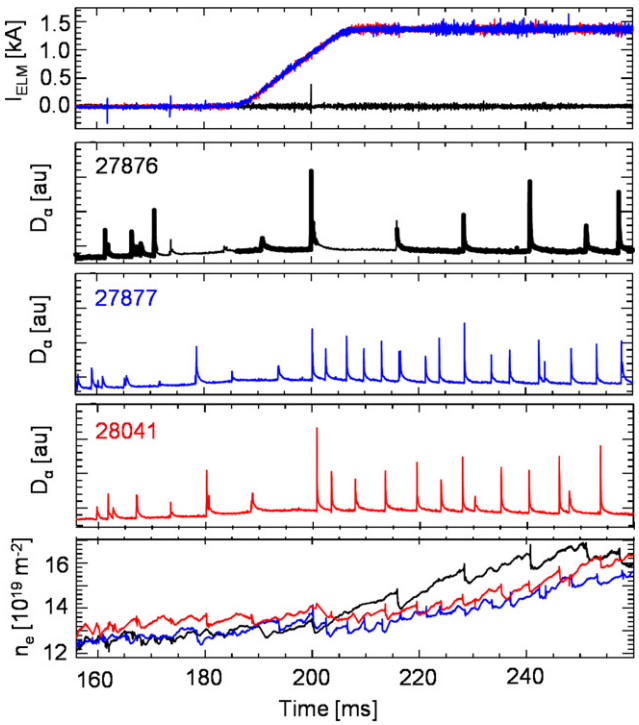

Figure 2. The current in the in-vessel coils, the D_α emission and the line-integrated electron density in MAST discharges 27876 (no RMP), 27877 (60° phase of $n = 3$ RMP) and 28041 (0° phase of $n = 3$ RMP). A clear increase in ELM frequency is observed for either phase of the $n = 3$ applied magnetic perturbation.

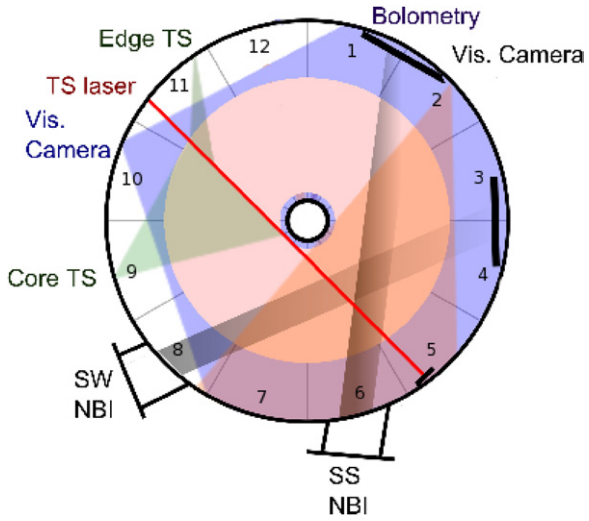

Figure 3. A schematic of the toroidal arrangement of some of the high-resolution diagnostics on MAST. Particularly useful for measurement of the plasma edge displacement are (clockwise from top) the linear visible-imaging camera with a viewing tangency plane in sector 12; the charge-exchange recombination spectroscopy which views the neutral beam from sector 6; the RGB filtered camera viewing a tangency plane in sector 7; the photron camera viewing sector 8; the visible-light camera with a tangency plane in sector 9; and the TS diagnostic viewing the laser in sector 11.

diagnostic which has a lens in sector nine viewing the laser beam in sector eleven.

The recently upgraded TS system on MAST [36], with radial resolution <10 mm and the possibility of temporal resolution of 1 μs, has allowed detailed analysis of the electron density and temperature profiles when magnetic perturbations are applied. The system is designed to measure at high spatial resolution and achieve low systematic and random errors, allowing observation of changes in the gradients over narrow regions associated with the edge pedestal.

Linear CCD cameras are used to measure D_α light from the plasma boundary, generated by plasma electron-impact excitation of the neutral deuterium gas in the vacuum vessel. The cameras are mounted at the horizontal midplane and oriented such that the pixel array spans the plasma boundary at both the high-field side and low-field side. The data are analysed by calculating the path length of camera pixel lines of sight through a radial mesh, extended in the toroidal direction to calculate a geometry matrix. A singular value decomposition algorithm is applied to the camera data and the geometry matrix in order to calculate the plasma D_α emissivity as a function of major radius. Two CCD cameras at neighbouring toroidal locations directly image visible-light photons using wide field-of-view lenses to image the interior of MAST. The data analysis procedure consisted of determining the camera location by finding the location of known features inside the vessel in the image plane within a 3D co-ordinate system. The camera location and field of view are then used to calculate the radius at which camera lines of sight are tangent to flux surfaces to give the local plasma brightness as a function of major radius. In all cases, the toroidal location at which the measurement is taken is assumed to be where camera lines of sight are tangent to the plasma boundary. There is some uncertainty in constraining the position of the edge of the plasma from the peak of the D_α emission [37] although qualitative differences between the different phases of applied magnetic perturbations are reliable.

The RGB filtered imaging diagnostic [38] is located 20.2 cm above the equatorial midplane. This diagnostic has a single iris, which filters all light through narrow, multi-spectral bandpass filters. Colour CCD sensors are used to measure the absolute intensity of six pre-selected emissions at medium frame-rates ($<$210 Hz). It has a wide circular field of view from the MAST-vertical axis to the outboard impact parameter value of $R = 1.64$ m with average pixel–pixel tangency separation of 2.5 mm and also measures spatially localized impurity-CX emissions from neutral beams. The spectral bandpass for the red channel presented here is the un-shifted D_α.

3. Measuring the three-dimensional displacement of the plasma equilibrium

Since there are twelve lower in-vessel coils in MAST, the phase of the $n = 3$ applied field can easily be changed in 30° quanta. In order to maximize the measurable perturbation of the edge of the plasma, two phases of an $n = 3$ RMP were applied with 60° between them, as illustrated in a cartoon in figure 4. This shows that the two offset phases of an $n = 3$ field would be expected to lead to the largest relative displacements in sectors 1,3,5,7,9 and 11, whilst exhibiting no relative displacement at other sectors. This has the added benefit that the position controller does not significantly correct for the distortion due to the applied RMPs as it is constrained by

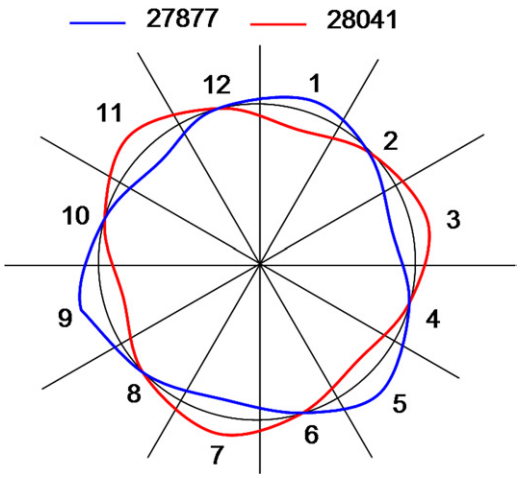

Figure 4. A cartoon showing an $n = 3$ displacement to the plasma edge with 0° phase in discharge 28041 (red line) compared with 60° in discharge 27877 (blue line). The corrugation in this cartoon is artificially large to exemplify the nature of the perturbations and should not be construed as an absolute displacement.

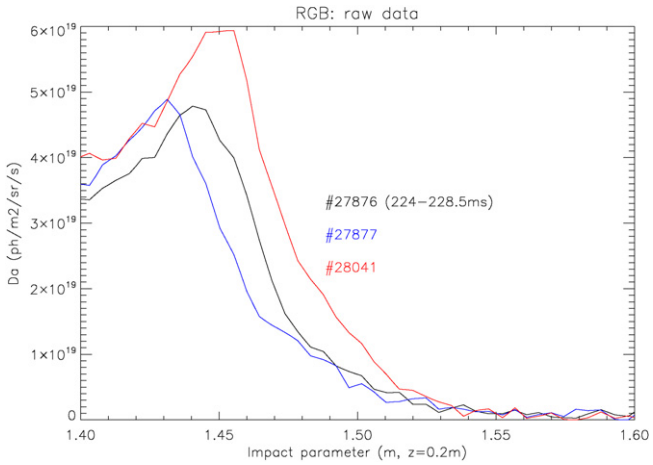

Figure 5. The impact radius of RGB emission at $Z = +0.2$ m for discharges 27877 (60°$n = 3$ RMP) and 28041 (0°$n = 3$ RMP) compared with shot 27876 (no applied field). The $n = 3$ fields clearly cause an inward and outward displacement in the tangency plane of the RGB camera, respectively.

measurements of the plasma position in a sector experiencing a null in displacement for both phases of applied field. A small $n = 0$ offset cannot be completely excluded due to the position controller response, though this would be expected to result in a systematic offset in the diagnostic measurements in other toroidal locations. In these MAST experiments, the plasma current was $I_p = 550$ kA, the toroidal field was $B_{T0} = 0.41$ T, $n_e \approx 3 \times 10^{19}$ m^{-3}, the NBI heating power was $P_{NBI} = 3.8$ MW, the normalized pressure was $\beta_N = \beta aB/I = 4.2$ and the safety factor at the 95th percentile of poloidal flux was $q_{95} = 7.2$. The maximum RMP field is applied in both phases of the RMP, $I_{RMP} = 5.6$ kAt, whilst the intrinsic error field, which is primarily $n = 1$ toroidal periodicity, is corrected with approximately (time-varying) -500 A and -150 A in the ex-vessel error field correction coils in sectors 5 and 11 and sectors 2 and 8 respectively, which is well below the predicted locked mode threshold in such MAST plasmas [32]. The application of $n = 3$ RMPs leads to significant ELM mitigation, with the frequency increasing substantially and the energy loss per ELM dropping commensurately. In discharge 27877, an $n = 3$ RMP with 60° phase is applied, whilst in discharge 28041, the phase of the $n = 3$ RMP is 0°, which can both be compared with shot 27876 which is an identical plasma without applied RMPs. The effect of RMPs on the ELM behaviour in these three MAST discharges can be seen in figure 2.

When RMPs are applied, the separatrix is deformed and the magnetic field near the edge of the plasma has stochastic regions. This makes the definition of the 'plasma boundary' somewhat more complicated. In the analysis that follows, we take the radial position of the boundary on each diagnostic to be determined in the same way in the axisymmetric case, for instance, for the TS diagnostic we assume the plasma boundary is at the position where the electron temperature is 40 eV. Of course, this does not account for any effect of the ergodic region upon heat or particle transport, but using this convention then allows comparison of the various models with the raw data.

The impact radius of the RGB emission (at $Z = +0.2$ m) in sector 7, the peak of which measures the position of the plasma edge, is shown in figure 5. It is evident that the edge of the plasma in shot 27877, measured to be at $R_{RGB}^{27877} = 1.46$ m is distorted inwards compared with the reference shot $R_{RGB}^{27876} = 1.47$ m, which itself is inside the 0° RMP case where $R_{RGB}^{28041} = 1.485$ m.

The cartoon in figure 4 suggests that the radial position of the plasma boundary measured by the RGB camera in sector 7 should be equal to that seen by the TS diagnostic measurements in sector 11. Figure 6 shows the plasma electron temperature and density measured by the TS. It is clear that, once more, the radial position of the plasma boundary for the 60° $n = 3$ RMP phase at $R_{TS}^{27877} = 1.46$ m is inside the reference plasma, $R_{TS}^{27876} = 1.47$ m, which is in turn inside the 0° RMP phase, $R_{TS}^{28041} = 1.485$ m. Not only is the trend the same, but good quantitative agreement is found between these two diagnostics. Furthermore, encouragingly, the midplane outboard radial position for the plasma without applied RMPs is consistently measured at $R_{noRMP} \approx 1.47$ m, a result which is further validated on four more diagnostics.

Finally, according to sketch 4 the plasma displacement in sector 9 ought to show the opposite phase dependence if a true $n = 3$ periodicity has corrugated the plasma edge. Figure 7 shows the D_α light measured by the fast visible camera as a function of tangency radius at the midplane with a tangency plane approximately in sector 9. In this case, the radial position of the plasma boundary for the 0° $n = 3$ RMP phase at $R_{Phantom}^{28041} = 1.465$ m is now inside the reference case, $R_{Phantom}^{27876} = 1.47$ m, whilst the 60° phase is now outside the reference case, $R_{Phantom}^{27877} = 1.48$ m. The amplitude of the perturbation is found to be smaller than in other toroidal sectors, though the relative phase of the displacement matches that expected in figure 4. This can be partially explained by the tangency plane of the camera being slightly toroidally displaced from the position of maximum edge corrugation. Here, the exposure time of the camera was 2 μs whilst the

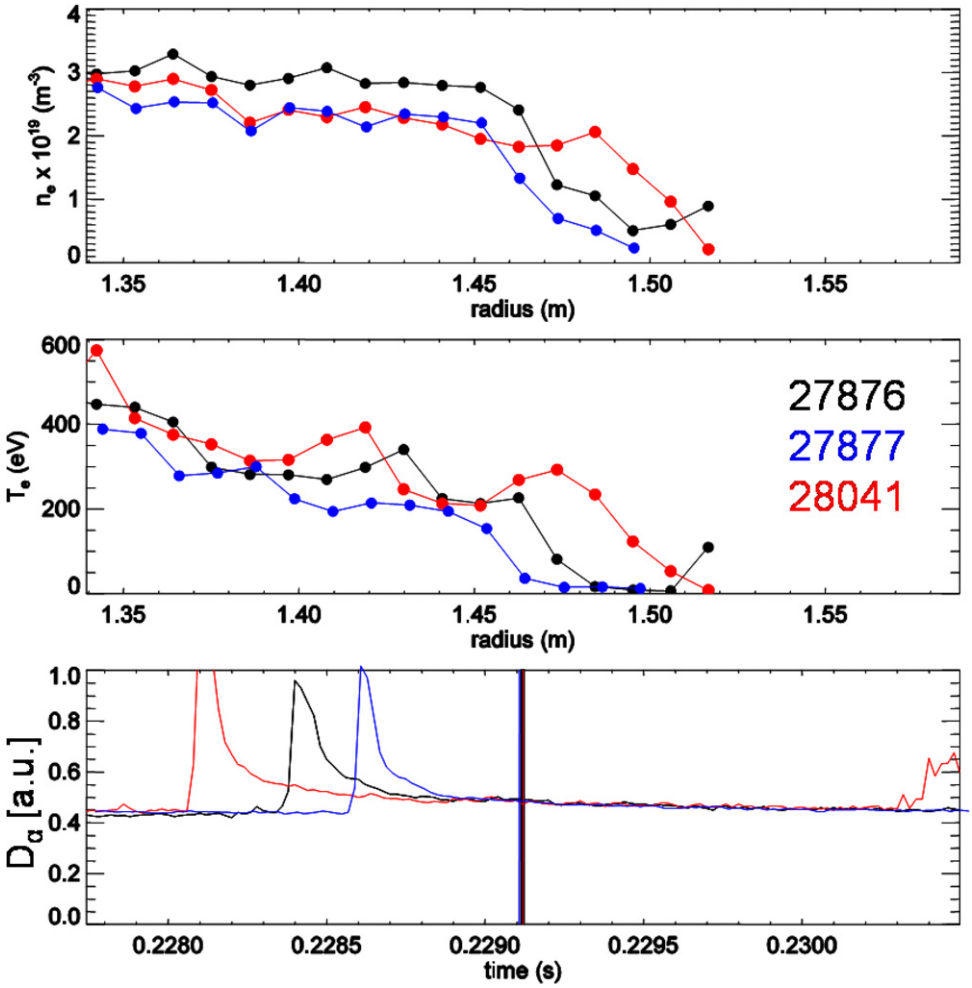

Figure 6. The electron temperature and density radial profiles in the edge region measured by the TS diagnostic at $Z = +0.015$ m and the D_α emission for discharges 27877 ($60°n = 3$ RMP) and 28041 ($0°n = 3$ RMP) compared with shot 27876 (no applied field). The $n = 3$ fields clearly cause an inward and outward displacement of the midplane plasma edge in the TS laser plane, respectively.

temporal resolution was 500 Hz. The spatial resolution is approximately 3 mm. The position of the plasma edge is found during a quiescent inter-ELM period (at 266 ms for shot 27876, 267 ms for shot 27877 and 266 ms for shot 28041). The plasma position for discharge 27876 when no magnetic perturbation is applied is found using a camera viewing the adjacent sector to the other two shots as unfortunately no camera data was available in the same sector for the coils-off shot. Since the plasma is nominally axisymmetric in the absence of magnetic perturbations, this comparison is reasonable.

The radial position of the plasma boundary for six different high-resolution diagnostics when the two phases of RMPs are applied (compared with a reference plasma in the absence of non-axisymmetric applied fields) is shown in figure 8. The expected toroidal phase dependence from figure 4 (with arbitrary amplitude) is added to guide the eye. It is clear that not only is there a different dependence of the edge corrugation in the two phases of the applied field, the toroidal variation follows the expected $n = 3$ periodicity symptomatic of the RMP applied. Furthermore, the amplitude of the displacement is found to be in good agreement on a number of different diagnostics and is approximately 3 cm between extrema, which represents more than 5% of the minor radius.

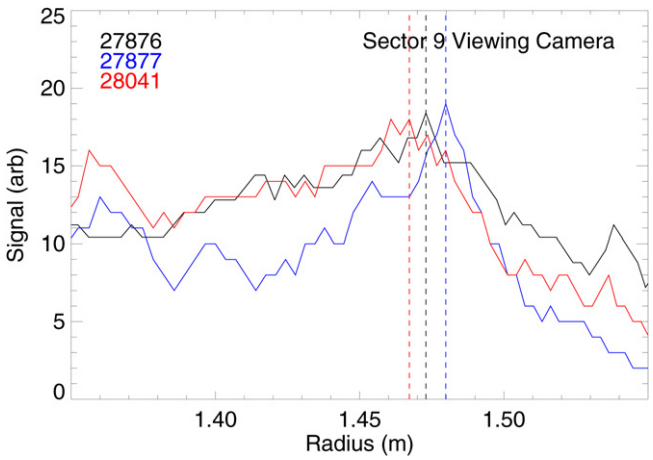

Figure 7. The plasma edge found from the Phantom camera at $Z = 0$ for discharges 27877 ($60°n = 3$ RMP) and 28041 ($0°n = 3$ RMP) compared with the coil-off case for discharge 27876. The $n = 3$ fields clearly causes a displacement of 2 cm between these phases of applied fields in the tangency plane of the colour camera.

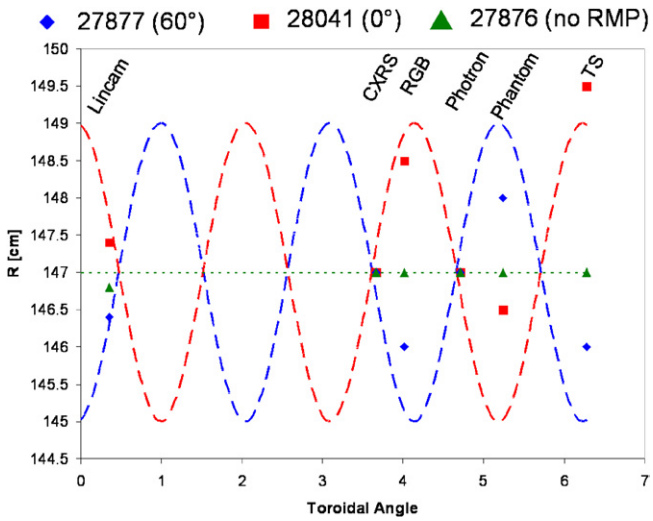

Figure 8. The measured plasma edge position as a function of toroidal angle when two phases of $n = 3$ field are applied in different MAST plasmas. (All diagnostics measure at the vertical midplane except for RGB which measures in the plane $Z = 0.2m$). Also plotted to guide the eye are two phases of an ideal $n = 3$ perturbation (blue line = 60° phase and red line = 0° phase) with the unperturbed position assumed to be the average measured in shot 27876 when no RMP is applied.

4. Numerical calculation of three-dimensional plasma equilibrium

The measured corrugation of the plasma edge discussed in section 3 can be compared with numerical reconstruction of the non-axisymmetric plasma equilibrium using the ANIMEC code [33]. The ANIMEC code is based upon the VMEC code [34] widely used in stellarator equilibrium simulation. ANIMEC assumes ideal nested flux surfaces and does not take into account either plasma screening of the applied field, nor any plasma amplification of the RMPs. Nonetheless, it is interesting to compare the predicted amplitude of the perturbation of the edge with the measured corrugation.

Before doing a full 3D plasma equilibrium reconstruction, we firstly consider the magnetic field perturbations expected using a vacuum field line tracing code, ERGOS [35]. A two-dimensional contour plot of the connection length of the field lines to the divertor targets as a function of toroidal angle is shown in 9. Each field line is traced for 200 toroidal turns or until it reaches the divertor target. They are coloured by the minimum normalized flux that the field line experiences during its trajectory. Figure 9(a) shows the vacuum magnetic field structure when an $n = 3$ RMP is applied to a double-null MAST discharge, whereas figure 9(b) shows how the field is perturbed when the intrinsic error field is also added. It is impossible to quantify an edge displacement in vacuum field modelling where the plasma boundary is no longer a discrete quantity as the magnetic field is ergodic. However, the distance from the original separatrix position, $R = 1.481$ m, to the most extreme radial position of a field line that experiences at least one toroidal turn within $\psi_N < 1$ is less than 1 cm, smaller than that experienced experimentally, indicating the need to include the plasma response in the equilibrium reconstruction.

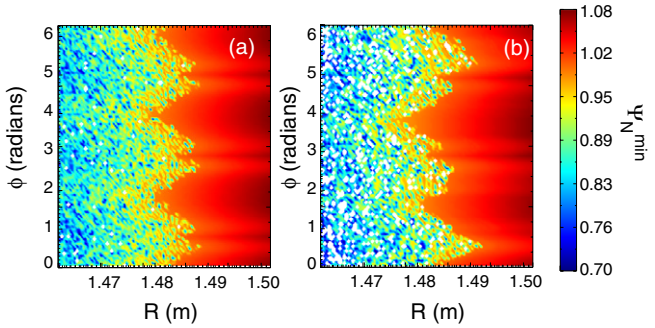

Figure 9. A two-dimensional contour plot of the connection length of the field lines to the divertor plates showing the vacuum field lines after 200 toroidal turns as a function of major radius and toroidal angle at $Z = 0$. The colour shows the minimum flux surface that each field line experiences during its trajectory. (a) The vacuum field from the poloidal field coils and the in-vessel RMPs, and (b) with the intrinsic error field also included. When no RMPs are applied, the separatrix is at $R = 1.481$ m. In both cases, the edge displacement is sub-centimetre.

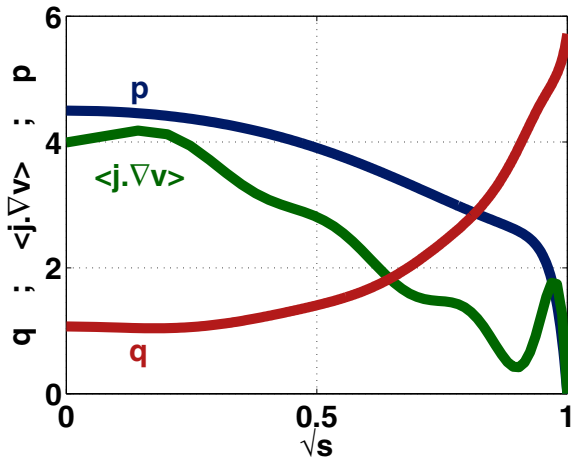

Figure 10. The equilibrium safety factor, flux-surface averaged toroidal current density and pressure profiles employed in the ANIMEC equilibrium reconstruction as a function of the minor radius, here expressed as the square root of the toroidal magnetic flux.

Figure 10 shows the current density, pressure and safety factor profiles used in the ANIMEC reconstruction. The pressure profile is taken from TS measurement of the electron temperature and density, assuming that $T_i = T_e$ with a clear bootstrap current peak present in the pedestal. ANIMEC is run in a free boundary mode and uses the coil configuration illustrated in figure 1.

The major radius of the edge of the plasma at the midplane with and without RMPs applied is shown in figure 11. In the absence of RMPs there is a small $n = 12$ displacement due to the toroidal field ripple, with $n = 1, 2, 3$ on top as a result of residual error fields. The amplitude of this ripple is below the spatial resolution of any of the diagnostics. The error fields are unknown, and whilst there is evidence that they result in a non-axisymmetry of MAST plasmas, it is not expected that they influence at least the qualitative results presented here. The error field included in the ERGOS simulations, which is the best estimate of the intrinsic error field in MAST, shows that the RMPs give the dominant effect on the edge corrugation,

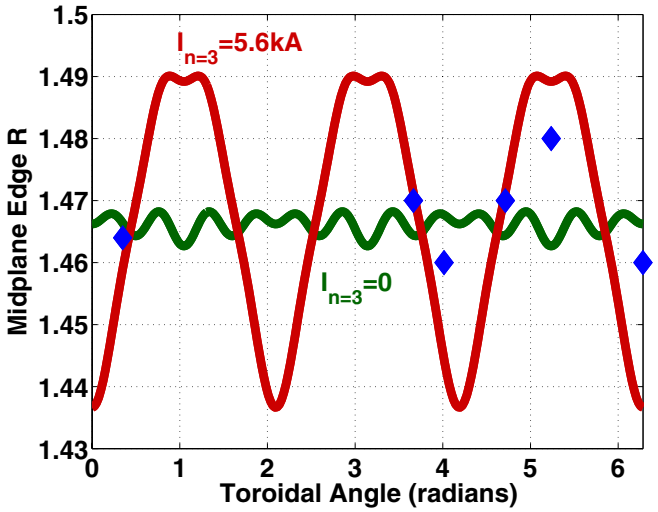

Figure 11. The plasma edge at the midplane predicted by ANIMEC when the applied RMP is 0 kAt and 5.6 kAt (i.e. full field). There is an $n = 12$ displacement arising from toroidal field ripple without RMPs, and a clear $n = 3$ displacement when RMPs are applied, with the residual toroidal field non-axisymmetry responsible for the secondary structure. Also shown is the diagnostic data from figure 8 for this phase of applied field.

justifying the absence of the full treatment in ANIMEC. When an $n = 3$ RMP is applied, the edge of the plasma is predicted to experience a corrugation of the order of 2.5 cm from its initial position, with a 5 cm shift of the plasma edge between the extrema. This is in relatively good agreement with the order of magnitude of the experimentally observed corrugation despite the absence of islands or screening in the modelling.

Figure 12(a) shows the shape of the plasma boundary predicted by ANIMEC at two different toroidal locations when the $n = 3$ RMP is applied. As well as causing a corrugation of the midplane position, the RMP also affects the plasma shape. This is also observed experimentally as the shape of the plasma changes with different phases of the applied field. Figure 12(b) shows the difference between two frames measured by the visible-imaging camera, one with 0° applied $n = 3$ RMP and the other with 60° phase. The boundary was calculated using the part of the camera image from the X-point going outboard, and then finding the maximum brightness for each row of pixels in the camera image, and recording the (R, Z) location of where the brightest pixel is tangent to circular flux surfaces. A similar off-midplane displacement is observed in the visible imaging as that predicted by numerical equilibrium reconstruction. Whilst the 60° phase of the applied perturbation causes the largest displacement at the midplane, it causes less displacement off-midplane. This is replicated by the ANIMEC equilibrium reconstruction.

The interaction between the plasma response and the separatrix manifolds is a matter of present research, such as local resonant screening effects [42] or how unstable manifolds form helical field-aligned lobes to facilitate ballooning instability [43]; such physics is of course important for complete modelling of the 3D equilibrium ensuing from applied RMPs. If plasma screening of the applied fields by rotation or magnetic shear were included one would expect the numerical reconstruction to predict a reduced corrugation, which may yield even better agreement with the experimental data. Including the plasma response to the applied fields in the equilibrium reconstruction, as carried out using ANIMEC in figure 11, gives an enhanced plasma corrugation compared with the vacuum field modelling in figure 9 and leads to improved agreement with the experimental data. Work is underway [44] to simulate DIII-D plasmas when RMPs are applied using the PIES code [45] which relaxes the nested flux-surface constraint of the VMEC reconstruction. This allows for the presence of magnetic islands and stochastic regions. Furthermore, it should be noted that the ERGOS modelling only accounts for the vacuum field line behaviour, and may not be representative of the confined plasma profiles; plasma transport in 3D and when open field lines exist in the pedestal region is very non-trivial, and an area of current research [46, 47]. Only by including this complex relationship between 3D transport in the presence of stochastic fields, plasma response interaction with separatrix manifolds and the 3D corrugation effects on a resistive equilibrium can one rigorously compare numerical simulation with the experimental measurements.

5. Discussion and conclusions

The most widely reported explanation for ELM suppression is that the application of RMPs induces a stochastic magnetic field giving rise to enhanced heat and particle transport, which in turn degrades the pressure gradient in the pedestal to below the level required to trigger an ELM [6]. However, the increase in ELM frequency caused by RMPs is harder to explain through this mechanism. Axisymmetric stability analyses of plasmas exhibiting ELM mitigation by RMPs typically find that peeling–ballooning stability is considerably enhanced [12], in contrast to the increase in ELM frequency observed. Understanding this dichotomy in the empirical effect of RMPs—either a stabilization of the ELMs by reducing the pressure gradient or a marked destabilization despite a reduction in pressure gradient—is key to understanding how RMPs control ELMs.

Recent three-dimensional electron cyclotron emission imaging of ELMs on KSTAR has shown that there is a strong toroidal asymmetry of ELM filaments [39]. Each ELM filament is seen to occur as discrete bursting fingers with different toroidal locations. This implies that a mechanism that changes the local ELM stability at any given toroidal location would affect ELM behaviour. This could be one explanation for the ELM mitigation observed on MAST [15, 18], whereby ELMs are destabilized and become more frequent with smaller amplitude. As an example, ballooning mode stability in a three-dimensional equilibrium has been modelled using the TERPSICHORE code [40] when a sawtooth crash leads to steep local temperature gradients with $n = 1$ toroidal periodicity in MAST [41]. It is found that in certain toroidal positions the $n = \infty$ ballooning stability is significantly degraded as the pressure surfaces are piled up, whilst in other locations ballooning stability is enhanced. A similar mechanism is likely to apply with the $n = 3$ perturbation to the edge pedestal presented in this paper, and the stability of such equilibria will

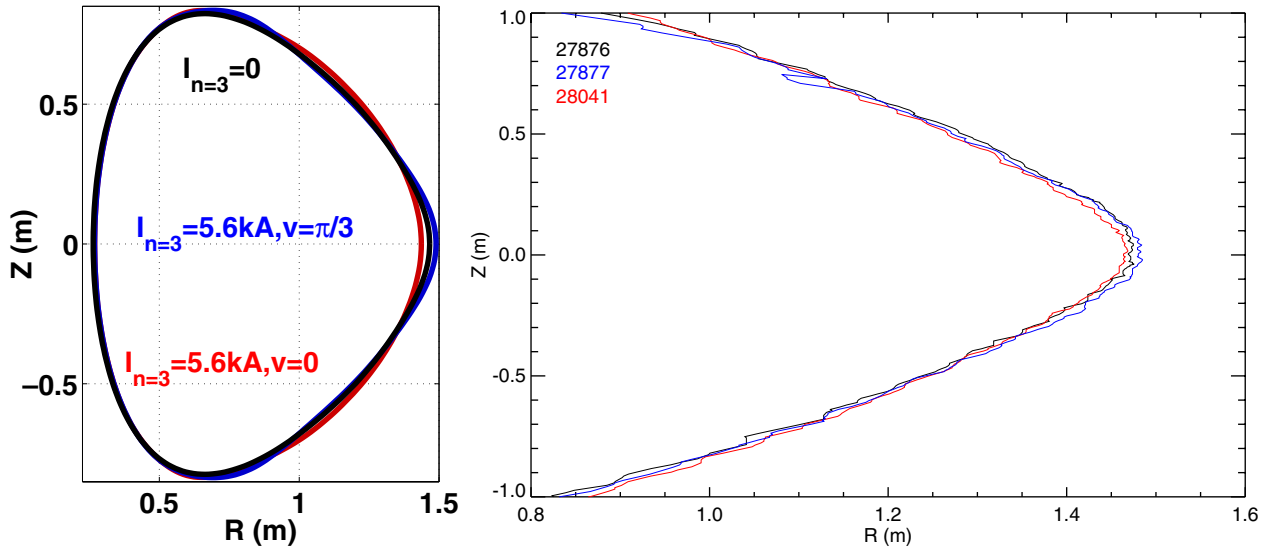

Figure 12. (*a*) The plasma boundary shape predicted by ANIMEC when the applied RMP is 0 kAt and 5.6 kAt (i.e. full field) at two toroidal positions 60° apart. (*b*) An image subtraction showing the difference in the plasma shape between two phases of the applied $n = 3$ RMP which are 60° apart.

be the subject of future work. Infinite-*n* stability analysis of a three-dimensional NSTX plasma when RMPs were applied found little change in the ballooning stability boundary [31]. However, in that work the displacement of the edge plasma was an order of magnitude smaller than that presented here, no doubt affected by the very different geometry of the coil sets which apply RMPs in MAST (similar to that in ITER) compared with that in NSTX.

The fact that the corrugation of the plasma edge at RMP fields required to mitigate the ELMs is of the order of 5% of the minor radius has strong implications for plasma exhaust schemes and plasma wall interactions. In order to consider rigorously how RMPs will affect plasma wall interactions in future devices such as ITER, a three-dimensional plasma surface interaction analysis is required, as highlighted in [46]. It is also important to understand how such corrugated plasmas will influence the heat loads on the plasma facing components in highly radiating plasmas such as ITER and the implications this has for restriction of the specification of RMP ELM control schemes.

To conclude, high spatial resolution measurements have been made of the displacement of the plasma boundary when resonant magnetic field perturbations are applied to H-mode MAST plasmas for ELM control. The plasma is found to be corrugated with a toroidal periodicity according to that of the applied non-axisymmetric field. The amplitude of the plasma corrugation is in good agreement with that predicted by three-dimensional equilibrium reconstruction. This is likely to locally affect peeling–ballooning stability—which will be the focus of future work—and may offer an explanation for the destabilization of finite-*n* peeling–ballooning modes hypothesized to be manifest as an increase in ELM frequency when RMPs are applied.

Acknowledgments

This work was partly funded by the RCUK Energy Programme under grant EP/I501045, the European Communities under the contract of Association between EURATOM and CCFE. The views and opinions expressed herein do not necessarily reflect those of the European Commission.

References

[1] Connor J W *etal* 1998 *Plasma Phys. Control. Fusion* **40** 531
[2] Snyder P B *et al* 2002 *Phys. Plasmas* **9** 2037
[3] Wilson H R *et al* 2006 *Plasma Phys. Control. Fusion* **48** A71
[4] Suttrop W 2000 *Plasma Phys. Control. Fusion* **42** A1
[5] Loarte A *et al* 2003 *Plasma Phys. Control. Fusion* **45** 1594
[6] Evans T *et al* 2004 *Phys. Rev. Lett.* **92** 235003
[7] Evans T *et al* 2008 *Nucl. Fusion* **48** 024002
[8] Jeon Y M *et al* 2011 *Proc. 53rd Annual Meeting of Division of Plasma Physics (Salt Lake City, UT)* (New York: AIP) T04.00005
[9] Suttrop W *et al* 2011 *Phys. Rev. Lett.* **106** 225004
[10] Kirk A *et al* 2011 *Plasma Phys. Control. Fusion* **53** 065011
[11] Liang Y *et al* 2010 *Nucl. Fusion* **50** 025013
[12] Saarelma S *et al* 2011 *Plasma Phys. Control. Fusion* **53** 085009
[13] Snyder P B *et al* 2007 *Nucl. Fusion* **47** 961
[14] Osborne T H *et al* 2008 *J. Phys:. Conf. Ser.* **123** 012014
[15] Chapman I T *et al* 2012 Towards understanding understanding ELM mitigation: the effect of lobe structures near the X-point on ELM stability *Nucl. Fusion* submitted
[16] Evans T *et al* 2005 *J. Phys:. Conf. Ser.* **7** 174
[17] Wingen A *et al* 2009 *Nucl. Fusion* **49** 055027
[18] Kirk A *et al* 2012 *Phys. Rev. Lett.* **108** 255003
[19] Jakubowski M W *et al* 2009 *Nucl. Fusion* **49** 095013
[20] Nardon E *et al* 2011 *J. Nucl. Mater.* **415** S914
[21] Cahyna P *et al* 2011 *J. Nucl. Mater.* **415** S927
[22] Schmitz O *et al* 2008 *Plasma Phys. Control. Fusion* **50** 124029
[23] Ahn J-W *et al* 2010 *Nucl. Fusion* **50** 045010
[24] Lao L *et al* 2005 *Proc. 47th Annual Meeting of Division of Plasma Physics (Denver, CO)* (New York: AIP) CP1.00034
[25] Fischer R *et al* 2011 Effect of non-axisymmetric magnetic perturbations on profiles at ASDEX Upgrade *38th EPS Conf. on Plasma Physics (Strasbourg, France)* P1.072 (http://ocs.ciemat.es/EPS2011PAP/pdf/P1.072.pdf)

[26] Fuchs J C *et al* 2011 *38th EPS Conf. on Plasma Physics (Strasbourg, France)* P1.090
[27] Chapman I T *et al* 2007 *Nucl. Fusion* **47** L36
[28] Lanctot M J *et al* 2011 *Phys. Plasmas* **18** 056121
[29] Wiegmann C *et al* 2009 *Proc. 37th European Physical Society Conf. Plasma Physics (Sofia, Bulgaria)*
[30] Wiegmann C *et al* 2008 *Proc. ITC18 (Toki)* P1-13
[31] Canik J *et al* 2012 *Nucl. Fusion* **52** 054004
[32] Howell D F, Hender T C and Cunningham G 2007 *Nucl. Fusion* **47** 1336
[33] Cooper W A *et al* 2009 *Comput. Phys. Commun.* **180** 1524
[34] Hirshman S P and Lee D K 1986 *Comput. Phys. Commun.* **43** 143
[35] Nardon E *et al* 2007 *J. Nucl. Mater.* **363** 1071
[36] Scannell R *et al* 2008 *Rev. Sci. Instrum.* **79** 10E730
[37] Tournianski M R *et al* 2003 *Rev. Sci. Instrum.* **74** 2089
[38] Patel A R *et al* 2004 *Rev. Sci. Instrum.* **75** 4145
[39] Yun G S *et al* 2011 *Phys. Rev. Lett.* **107** 045004
[40] Anderson D V *et al* 1990 *Int. J. Supercomput. Appl.* **4** 34
[41] Chapman I T *et al* 2010 *Phys. Rev. Lett.* **105** 255002
[42] Cahyna P *et al* 2011 *J. Nucl. Mater.* **415** S927
[43] Sugiyama L E *et al* 2010 *Phys. Plasmas* **17** 062505
[44] Lazerson S *et al* 2011 *Proc. 53rd Annual Meeting of Division of Plasma Physics (Salt Lake City, UT)* (New York: AIP) T04.00007
[45] Reiman A and Greenside 1986 *Comput. Phys. Commun.* **43** 157
[46] Schmitz O *et al* 2011 *J. Nucl. Mater.* **415** 886
[47] Frerichs H *et al* 2010 *Nucl. Fusion* **50** 034004